2D luminescence imaging of pH in vivo

Stephan Schreml[a,1,2], Robert J. Meier[b,1], Otto S. Wolfbeis[b], Michael Landthaler[a], Rolf-Markus Szeimies[a], and Philipp Babilas[a,2]

[a]Department of Dermatology, University Hospital Regensburg, 93042 Regensburg, Germany; and [b]Institute of Analytical Chemistry, Chemo- and Biosensors, University of Regensburg, 93040 Regensburg, Germany

Luminescence imaging of biological parameters is an emerging field in biomedical sciences. Tools to study 2D pH distribution are needed to gain new insights into complex disease processes, such as wound healing and tumor metabolism. In recent years, luminescence-based methods for pH measurement have been developed. However, for in vivo applications, especially for studies on humans, biocompatibility and reliability under varying conditions have to be ensured. Here, we present a referenced luminescent sensor for 2D high-resolution imaging of pH in vivo. The ratiometric sensing scheme is based on time-domain luminescence imaging of FITC and ruthenium(II)tris-(4,7-diphenyl-1,10-phenanthroline). To create a biocompatible 2D sensor, these dyes were bound to or incorporated into microparticles (aminocellulose and polyacrylonitrile), and particles were immobilized in polyurethane hydrogel on transparent foils. We show sensor precision and validity by conducting in vitro and in vivo experiments, and we show the versatility in imaging pH during physiological and chronic cutaneous wound healing in humans. Implementation of this technique may open vistas in wound healing, tumor biology, and other biomedical fields.

hydrogen | sensors and probes | fluorescence | skin | dermatology

There is great interest in luminescence imaging of essential biological parameters, such as pH, pO_2, hydrogen peroxide (H_2O_2), and Ca^{2+}, at the moment (1–6). Recently, luminescence-based methods for pH measurement have been developed (7, 8). However, a method for in vivo studies on human subjects has not yet been realized. The major challenges for in vivo applications are that biocompatibility and reliability under varying conditions (illumination, oxygen, and temperature) have to be ensured. The standard tool for pH measurement, the glass electrode (9), is not approved for clinical use and only allows single-spot measurements, which makes 2D imaging impossible.

Multiple methods for pH imaging exist: ratiometric luminescent pH detection is a straightforward and referenced approach, which has been used, for instance, to measure intracellular pH. In these works, either combinations of dextran-conjugated indicator and reference dyes (fluorescein/tetramethylrhodamine and pHrodo/rhodamine-green) or seminaphtho-rhodafluor (SNARF) derivatives have been used (10–12). However, to obtain 2D images, either modifications of the optical system during measurements or the use of an image splitter are necessary to separate the signals. Ratiometric methods may suffer from Förster's fluorescence resonance energy transfer (FRET) and most importantly, from differential photobleaching of indicator/reference dyes. The latter problem may be avoided by using intrinsically referenced luminescence lifetime imaging (LLI) of one single pH indicator. LLI has been used for high-resolution 2D and 3D pH mapping in studies on cells, tissue samples, and artificial skin constructs (13–15). These techniques are, however, difficult to implement in studies on live human subjects because of long scanning times, highly sophisticated measurements setups (confocal microscope, laser, etc.), and the necessity of a spatially fixed sample. Furthermore, most scanning techniques are invasive, because the luminophores have to be in direct contact with the sample (15). Additionally, pH imaging probes based on ^{1}H, ^{31}P, and ^{13}C have

been developed for magnetic resonance spectroscopy (MRS) of tumor pH, but (i) the low sensitivity of spectroscopy, (ii) the oftentimes small pH-induced chemical shift of these agents, and (iii) the complex measurement system make it hard to create high-resolution images with precise pH values at clinical magnetic field strengths in routine clinical settings (16–18).

To date, no pH sensor exists that detects pH over a wide proton concentration range, allows for fast micro- and macroscopic 2D pH imaging, and is noninvasive and biocompatible for in vivo use on humans. We developed a 2D pH sensor that meets these requirements. The prerequisites include (i) the use of a referenced method, because in vivo conditions are quite variable, (ii) nontoxic and easily applicable materials, (iii) a dynamic range from pH 3 to 9, and (iv) a noninvasive method, allowing it to be suitable for clinical applications.

For in vitro characterization, we conducted calibration experiments under varying conditions (pO_2 and temperature changes) and studied the (spatio)temporal resolution. To evaluate the precision and validity in vivo, we measured the pH gradient in the stratum corneum (SC) after tape stripping of the SC on the volar forearm and compared the results with data obtained using the standard glass electrode. Additionally, we applied the sensor to a routine clinical problem (i.e., cutaneous wound healing) to show its potential and superiority compared with the glass electrode (9). We used split-thickness skin graft donor sites as standardized cutaneous wounds and measured the pH over the time course of physiological healing. To accent the potential for 2D imaging, we visualized the pH distribution within a chronic cutaneous wound. We chose cutaneous wound healing as the first in vivo application for the luminescent pH sensor, because the wound fluid (19) and its varying pH are known to greatly affect healing (20–22). Despite the fact that there are numerous new findings in wound healing (23), knowledge on basic clinical parameters like pH is still missing in the literature, which is obviously because of the lack of appropriate tools for 2D pH imaging in vivo. The importance to study basic biological parameters in wound healing is highlighted by the fact that H_2O_2 gradients have recently been found to be essential for immediate leukocyte recruitment to the wound site after tissue injury (5).

Additionally, pH has a major impact on the pathogenesis of chronic wounds, which often presents an interdisciplinary treatment challenge. Apart from the impact on the quality of life of the patients affected, chronic wounds are a fundamental economic burden (24). About one-third of the dermatological health

budget in the United States is spent on the treatment of chronic wounds, more than for all oncological indications (melanoma and nonmelanoma skin cancer) combined (24). Therefore, in vivo studies of the pH distribution in tumor growth and metabolism are expected to be among the future applications for the luminescent 2D pH sensor (25, 26).

This article shows the development, in vitro characterization, in vivo validation, and clinical application of a sensor for 2D luminescence imaging of pH in humans.

Results and Discussion

Luminescence Imaging of pH. Imaging of pH is challenging, because many of the pH-dependent luminophores exhibit luminescence lifetimes that are too short for LLI methods, which do not use microscopic scanning. To overcome this issue, we used time-domain dual lifetime referencing (tdDLR), a method previously described by our group (8). Two simultaneously excitable luminophores with different lifetimes were chosen, FITC (λ_{ex} = 495 nm, λ_{em} = 525 nm, singlet emission = fluorescence, <5-ns lifetime) as the indicator and ruthenium(II)tris-(4,7-diphenyl-1,10-phenanthroline) [Ru(dpp)$_3$; λ_{ex} = 441 nm, λ_{em} = 597 nm, triplet emission = phosphorescence, ~6-µs lifetime] as the reference (Fig. 1A). Both dyes can be excited at 460 nm with light emitting diodes (LED), which allows for imaging of pH in one single excitation–emission cycle. Luminescence was recorded using a time-gated charge-coupled device (CCD) camera with a 530-nm long-pass optical filter (Fig. 1B).
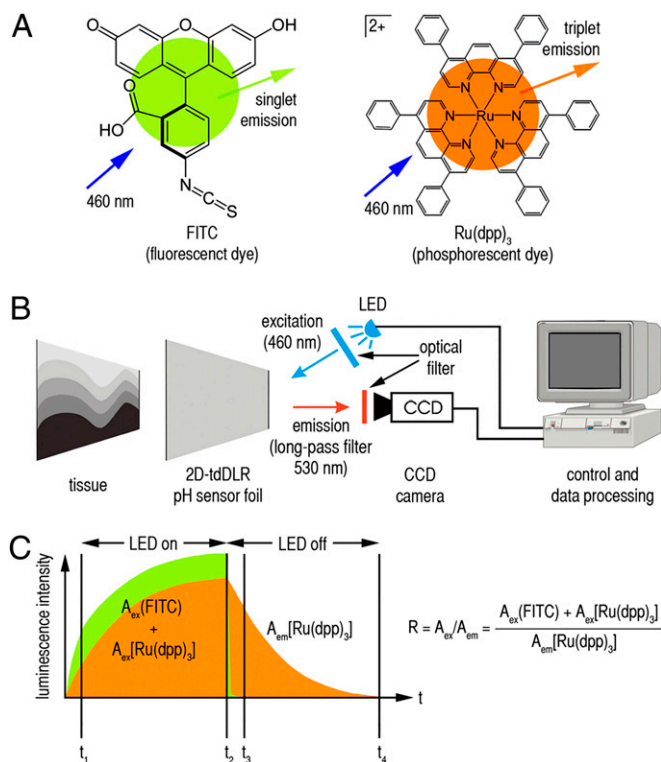
The long-lasting phosphorescence of Ru(dpp)$_3$ enables recording luminescence during the emission phase (LED off), whereas the combined luminescence of FITC and Ru(dpp)$_3$ is detected during excitation (LED on). Thus, the pH-dependent FITC signal is referenced to the pH-independent Ru(dpp)$_3$ signal. Luminescence intensity was integrated in two time gates: one during excitation (A_{ex}), and one during emission (A_{em}). Given the fact that, during excitation, the integrated signal intensity reflects the combination of FITC and Ru(dpp)$_3$ signals, A_{ex} is A_{ex}(FITC) + A_{ex}[Ru(dpp)$_3$]. However, 250 ns after turning the LED off, fluorescence of FITC has decayed, and only the phosphorescence signal of Ru(dpp)$_3$ is detected; therefore, A_{em} is A_{em}[Ru(dpp)$_3$] (Fig. 1C). The ratio R of A_{ex}/A_{em} denotes a referenced integrated signal intensity (8). Thus, little irregularities in particle distribution or illumination of the sensor do not alter the measured ratio R. This fact is a major advantage, especially if the density of the sensor particles differs locally or if illumination cannot be controlled as precisely as in a laboratory setting.

To calculate pH values based on the detected R, we calibrated each sensor and computed a five parametric sigmoidal fit according to (Eq. 1):

$$R = \frac{a}{b + \left(c^* e^{d^* pH} + t\right)} \quad [1]$$

This enables the measurement of pH over a wide proton concentration range, because the pseudolinear part of the calibration curve is not the only part used. From the respective calibration curve, pH is calculated by solving the equation for pH (Eq. 2):
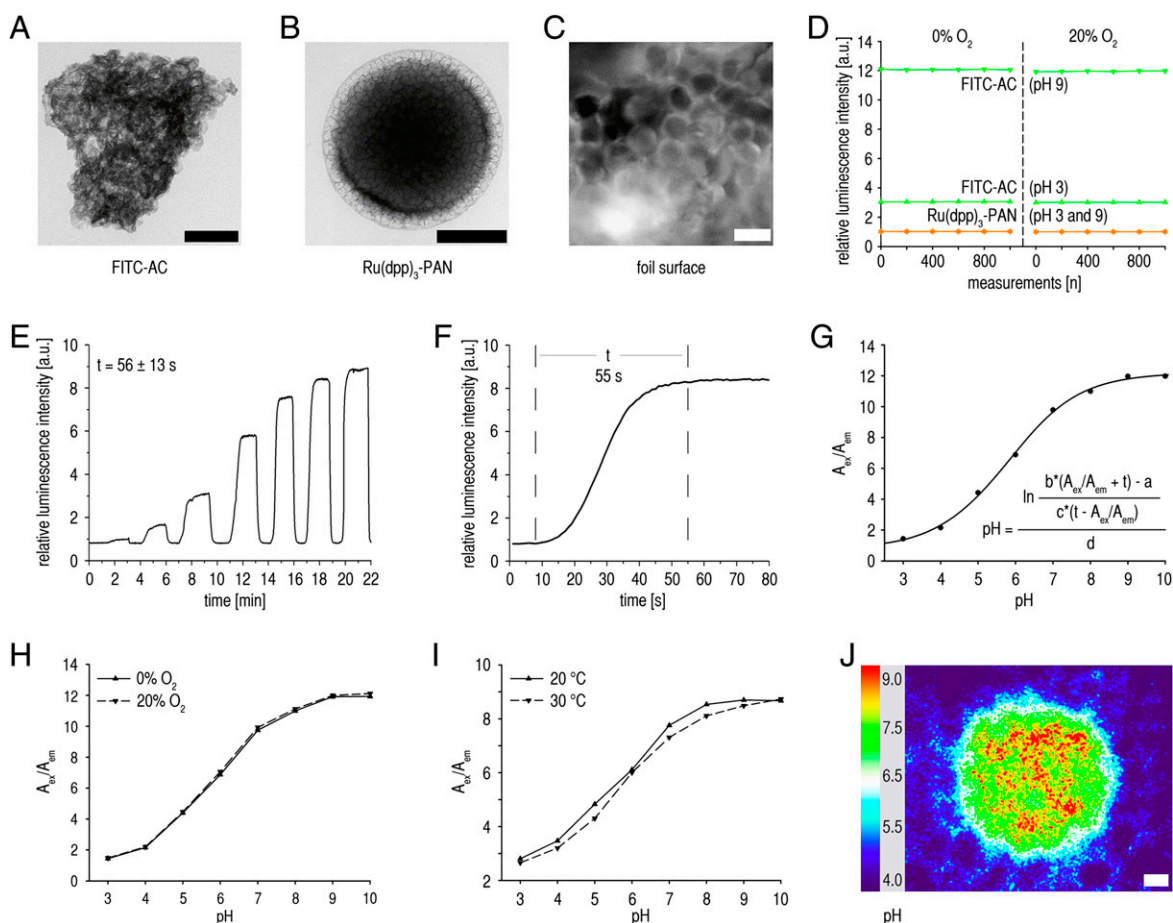
$$pH = \frac{\ln\left[\frac{b^*(R+t)-a}{c^*(t-R)}\right]}{d} \quad [2]$$

Material Design. In contrast to other methods, our noninvasive approach ensures high biocompatibility for in vivo use. A three-step safety system was introduced: (i) luminophores were covalently bound to or encapsulated in biologically inert particles to prevent leaching of the luminophores, (ii) particles were immobilized in a biocompatible matrix on transparent foils to prevent particle leakage into tissues (Fig. S1), and (iii) particles were synthesized to have a minimum size of 0.5 µm in diameter to hamper or at least to slow down the process of possible cellular uptake.

Therefore, FITC was covalently bound to aminocellulose (AC) particles (FITC-AC; 0.75–3 µm) (Fig. 2A), and Ru(dpp)$_3$ was physically entrapped (hydrophobic interactions) in polyacrylonitrile particles [Ru(dpp)$_3$-PAN; 0.5–1 µm] (Fig. 2B). Thus, leakage of dyes is prevented (Fig. S2 A–D). AC was chosen, because (i) it offers amino groups to covalently bind FITC, (ii) it is a hydrophilic polymer that allows fast proton diffusion for a quick sensor response, and (iii) FITC exhibits a high singlet quantum yield in hydrophilic environments ($\phi_{singlet}$ = 0.97 in H$_2$O) (27). The conjugation of FITC to AC shifts the pK$_a$ of fluorescein from 6.8 to 5.9. Residual amino groups of AC were blocked with acetic anhydride to remove surface charges that may alter sensor response. PAN is a hydrophobic polymer that is impermeable to oxygen, thus preventing the quenching of reference luminescence as well as the formation of reactive oxygen species (ROS), such as singlet oxygen (*Biocompatibility*). The encapsulation in PAN would also prevent FRET in case of a significant overlap between the luminescence spectra of certain dyes, but FRET is not an issue with the dyes used in this work.

Fig. 1. Dyes, measurement setup, and sensing scheme. (A) Chemical structure of the indicator dye FITC and the reference dye Ru(dpp)$_3$. (B) The sensor foil is applied to the tissue, protons diffuse into the sensor, and luminophores are excited (LED; λ_{ex} = 460 nm). Time-gated luminescence intensities are recorded (530-nm long-pass optical filter) with a CCD camera, and subsequently, data are processed. (C) During excitation, the combined luminescence intensity of FITC (green) and Ru(dpp)$_3$ (orange) is detected, whereas during the emission time gate, only the luminescence intensity of Ru(dpp)$_3$ is detected. Luminescence intensity is recorded and integrated in two time gates, one during excitation ($t_1 – t_2$; A_{ex}) and one during emission ($t_3 – t_4$, A_{em}). A ratio R of A_{ex}/A_{em} allows us to calculate pH from the respective five parametric calibration curve obtained for each sensor (Fig. 2G).

Fig. 2. In vitro characterization of the sensor particles and foils. (*A* and *B*) Transmission electron microscopic (TEM) images of (*A*) FITC bound to AC particles (FITC-AC) and (*B*) Ru(dpp)$_3$ incorporated into PAN particles [Ru(dpp)$_3$-PAN]. (Scale bars, 200 nm.) (*C*) Fluorescence microscopic image of a PVdC foil coated with FITC-AC sensor particles and Ru(dpp)$_3$-PAN reference particles (e.g., in the lower left corner) embedded in a polyurethane-hydrogel matrix. (Scale bar, 1 µm.) (*D*) Photostability. Relative luminescence intensities of FITC-AC (green) and Ru(dpp)$_3$-PAN (orange) during repeated measurements under varying oxygen and pH values. The vertical dashed line separates the experiments for 0% and 20% O$_2$. Relative luminescence intensities of Ru(dpp)$_3$-PAN are virtually identical for pHs 3 and 9. (*E* and *F*) Time trace of sensor response (a.u., arbitrary units) after defined pH variations (*E*) until 99% steady-state conditions for pH measurements were achieved (*t*, time until steady state = 56 ± 13 s; *n* = 10 sensors) and (*F*) a representative pH variation (*t*, mean ± SD; *n* = 10). (*G*) Sigmoidal calibration curve of the sensor. pH values may be calculated from the measured ratio *R* (A_{ex}/A_{em}) of integrated signal intensities during excitation (LED on; A_{ex}) and emission (LED off; A_{em}) by means of a five parametric sigmoidal equation. (*H* and *I*) Representative sensor calibration shows neither O$_2$ nor temperature dependency. (*J*) Spatial resolution shown by a representative visualization of a drop (pH 8) on a sensor foil impregnated in a solution of pH 4 after connecting the CCD camera to a microscope (Movie S1). (Scale bar, 10 µm.)

FITC-AC and Ru(dpp)$_3$-PAN particles were subsequently immobilized in a polyurethane-hydrogel matrix (thickness ~6 µm) on a transparent poly(vinylidene-chloride) foil (PVdC; thickness ~12 µm) to prevent leakage of particles (Fig. S2 *E* and *F*) and create a 2D sensor (spectra in Fig. S3). The sensors were sterilized during the fabrication process with ethanol in water (90% vol/vol) as the solvent for the hydrogel matrix. The PVdC support is transparent, inert, and flexible to be applicable to uneven surfaces. The transparency of the foils allows the observation of the underlying anatomical structures and the creation of exact overlay pictures (photographic and luminescence images) (Fig. S1). Before use, all sensor foils were inspected for gross irregularities or larger uncoated gaps by means of fluorescence microscopy (Fig. 2*C*).

In Vitro Characterization. A set of in vitro experiments served to characterize the sensor. For at least 1,000 measurement cycles, dyes show high photostability, even under different oxygen and pH conditions (Fig. 2*D*). Most importantly, the luminescence intensity ratio *R* remains almost unchanged (Fig. S4). Thus, the sensor produces reliable measurements, even during continuous imaging. To extend the shelf time of the sensor, foils were stored in optically opaque envelopes until use. To determine the time necessary for accurate pH measurements (proton diffusion through hydrogel matrix to FITC-AC particles), we conducted time trace studies that showed a 99% steady-state signal response after 56 ± 13 s (Fig. 2 *E* and *F*). Therefore, all subsequent measurements were done after 1.5 min. Calibration showed sigmoidal curves and reliable pH measurements within the pH range from at least 3 to 9 (Fig. 2*G*), which covers the range needed for clinical use. The sensor is independent of oxygen tension over a wide range (Fig. 2*H*). This independence is important, because O$_2$ is known to be a quencher of luminescence and may vary in clinical settings. Additionally, the response is virtually unaffected by temperature changes in the range encountered in clinical settings (Fig. 2*I*). The spatial resolution of the sensor foils was studied by coupling the CCD camera to a microscope. Using our setup, we found that differences in pH may be detected with a resolution of <5 µm (Fig. 2*J*). Continuous imaging showed that hardly any horizontal proton diffusion occurs in hydrogel, which would alter the resolution (Movie S1).

However, other microscopic imaging systems may allow higher resolution (28).

Biocompatibility. Dyes were bound to or encapsulated in inert polymer particles, and sensor particles were immobilized on PVdC foils (*Results and Discussion* and *Materials and Methods*), thus preventing dye and particle leakage into tissues. However, before use in an in vivo setting, potential cytotoxic effects were studied by exposure of human epidermal keratinocytes (HKs) and L929 fibroblasts to sensor particles. Cell viability was assessed with the 3-(4,5-dimethyl-2-thiazolyl)-2,5-diphenyl-tetrazolium-bromide (MTT) assay. Both particle types show no cytotoxicity (Figs. S5 and S6) and are not taken up by live cells (Figs. S7 and S8 and Movies S2–S5). Additionally, we showed that both types of microparticles do not lead to the formation of cytotoxic singlet oxygen, a member of the reactive oxygen species (ROS) family (Fig. S9). FITC does not effectively create singlet oxygen, because it is a poor triplet emitter ($\phi_{triplet}$ = 0.03 in H_2O) (27); Ru(dpp)$_3$ may not create singlet oxygen, because it is shielded by oxygen-impermeable PAN. The method described herein prevents direct exposure of tissues to the agents. In terms of safety, it has to be mentioned that fluorescein conjugates are routinely used in medical diagnostics, even as injectables (e.g., in fluorescence angiography) (29, 30).

In Vivo Validation. For luminescence imaging in vivo, sensor foils only remained on tissues for the duration of measurements (<5 min from application to image). To validate our method in vivo, we measured the pH gradient in the SC by tape stripping the SC on the volar forearm (31). A set of experiments on 10 volunteers served to evaluate the precision and validity of the sensor in vivo. Therefore, pH measurements were compared with data obtained with the glass electrode (9). The SC was gradually removed by multiple tape strippings, and a trans-SC pH gradient was found with luminescence imaging and electrodes (Fig. 3*A*). No significant differences in pH values were found between the two methods. A high level of precision was achieved for an in vivo setting, and the precision was similar for both methods [relative SD (RSD); RSD$_{tdDLR}$ = 4.32 ± 1.35%, RSD$_{electrode}$ = 4.53 ± 2.04%]. A Bland–Altmann mean difference plot (32) (Fig. 3*B*) was created for method comparison, showing excellent concordance (96% of the measurements were within the 95% confidence interval; Krippendorf coefficient K = 0.98). Hereby, we have proven that the pH sensor can be reliably used in an in vivo setting.

Luminescence Imaging of pH in Cutaneous Wound Healing. The sensor was then applied to a routine clinical problem (i.e., cutaneous wound healing) to show its potential and superiority compared with the glass electrode. We used split-thickness skin graft donor sites on the thighs of 10 patients as standardized cutaneous wounds because of the potential of pH to act as a diagnostic for healing. Basically, cutaneous wound healing comprises three major overlapping phases: inflammation, proliferation (tissue formation), and tissue remodeling (22, 33).

We found that pH continuously decreased during physiological healing and that no significant differences existed between the two methods (Fig. 3 *C* and *D*). Thereby, we were able to prove that the sensor is reliably applicable in a clinical setting, showing great promise as a tool to monitor pH in clinical routine.

Fig. 3. In vivo validation of the luminescent pH sensor. (*A* and *B*) SC pH gradient (*A*) on the volar forearm measured with luminescent pH sensors and a pH glass electrode. RSD amounted to 4.32 ± 1.35% for the sensor and 4.53 ± 2.04% for the glass electrode (mean ± SD; n = 10). The respective Bland–Altmann mean difference plot (*B*) shows 96% of measurements within the 95% confidence interval (CI), and the Krippendorf coefficient amounted to K = 0.98. (*C* and *D*) pH during physiological wound healing of split-thickness (~400 μm) skin-graft donor sites on the thigh (*C*) using luminescence imaging of pH and a pH glass electrode. pH gradually declined over the time course of physiological cutaneous wound healing, reflecting the reestablishment of the epidermal barrier. The respective Bland–Altmann mean difference plot (*D*) shows 93% of the measurements within the 95% CI, and the Krippendorf coefficient amounted to K = 0.89 (mean ± SD; n = 10; *P < 0.05, **P < 0.01).

The major advantage, however, is the capability of the sensor to yield 2D pH images, which is mandatory for the evaluation of spatially heterogeneous processes like wound healing or tumor biology. Representative photographs of split-skin donor site wounds are presented for days 1 (inflammation), 6 (granulation = fibroblast proliferation), and 14 (reepithelialization = keratinocyte migration and proliferation) after split-skin harvesting (Fig. 4 *A–C*). The pseudocolor images (Fig. 4 *E–G*) show local differences in pH during the wound-healing stages, and the transparency of the sensor foils enables the correlation of clinical and pseudocolor 2D pH images.

In chronic wound healing, a sustained inflammatory phase is supposed to prevent this stepwise process of wound closure (22, 33). To accent the potential for 2D pH imaging, the heterogeneity of pH within a chronic venous ulcer was visualized (Fig. 4 *D* and *H*). Within this chronic wound, extensive areas with pH values as detected in the inflammatory phase (red to yellow) are seen, thus indicating a sustained inflammatory phase. The intact surrounding skin (Fig. 4 *D* and *H*, shown in the upper left and right corners) is clearly demarcated by lower pH values.

Conclusions

In this work, we developed an optical pH sensor in vitro, which was validated in vivo, and we showed a noninvasive method for 2D and potential real-time pH imaging in vivo. We also present images of the pH distribution during acute and chronic wound healing. Extensive areas within a chronic wound showed similar pH values to those during the initial phase after wounding. Using the respective color code, the pseudocolor 2D pH images allow for the easy correlation of pH with the heterogeneous morphology of chronic wounds. Further studies of the 2D pH distribution in heterogeneous chronic wounds (24) aim at the development of a pattern recognition model (34, 35) to predict the course of cutaneous healing. Furthermore, the biocompatible sensor holds great potential for various clinical and laboratory applications, such as tumor biology (tumor microenvironment) (25, 26), the study of pH in dermatological conditions (e.g., epidermal barrier dysfunction in atopic dermatitis) (36), microbiology (e.g., imaging bacterial cultures) and food technology (37–39), and the monitoring of industrial production processes.

Materials and Methods

Microparticle Preparation. Ten milligrams (2% wt/wt) FITC (Sigma-Aldrich) was covalently conjugated to 500 mg AC particles (OptoSens) in 18 mL sodium bicarbonate buffer (50 mM, pH 9) to form FITC-AC particles (reaction time = 2 h). Residual amino groups on the particles were blocked with acetic anhydride (Ac$_2$O; Sigma-Aldrich); 100 mg AC was reacted with 200 mg Ac$_2$O in 10 mL ethanol for 12 h. Particles were washed (eight times with distilled water) and additionally filtered through centrifugation (10 min at $1,030 \times g$, EDA12; Hettich) after each washing step. Reference particles were synthesized by incorporating (2% wt/wt) Ru(dpp)$_3$ (Sigma-Aldrich) in PAN (Sigma-Aldrich) to form Ru(dpp)$_3$-PAN particles (40). We obtained particles by precipitating 250 mg PAN dissolved in 50 mL dimethylformamide with 70 mL distilled water (drop-wise addition, 1 mL·s^{-1}) and the subsequent addition of 20 mL Brine. Particles were washed (eight times with distilled water and four times with ethanol) and subsequently filtered through centrifugation (10 min at $1,030 \times g$) after each washing step. Reactions were conducted at room temperature, and particles were freeze-dried (Modulyo; IMA Edwards) for storage. Particle size was assessed with a LEO912 AB transmission electron microscope (Carl Zeiss).

Preparation of the Sensor Foils. FITC-AC (150 mg) and Ru(dpp)$_3$-PAN (50 mg) were mixed with 20 mL of a solution (5% wt/vol) consisting of polyurethane-hydrogel (type D4; Cardiotech International Inc.) in ethanol/water (90/10 vol/vol). This mixture was spread on a transparent PVdC foil (Saran plastic wrap; Dow Chemicals) with a K Control Coater model 101 knife-coating device (RK Print-Coat Instruments Ltd.) to form a 120-μm-thick film (41–43). After drying, the sensor layer was 6-μm thick. We controlled particle distribution on the foils by means of fluorescence microscopy (Axiotech; Carl Zeiss).

Time Response, Spectra, and Photostability. Experiments are described in *SI Materials and Methods*.

Luminescence Measurement and Calibration. The camera was combined with a light emitting 460 nm LED array (Luxeon V Star LXHL-LB5C 5W; Lumileds Lighting Company). To image 2D pH distribution, tdDLR measurements (8) were performed by means of an ImageX Time Gated Imaging system (TGI; Photonic Research Systems) with an integrated 12-bit CCD chip (640 × 480 pixels). Parameters were set as subtract background, 5-μs gate width, 0.25-μs delay time, 6-μs lamp pulse, 400-Hz recording frequency, and 100-ms integration time. We used a 530-nm long-pass OG530 glass filter (Schott) as an emission filter. Calculations and pseudocolor image processing were done with ImageX software (Microsoft Corporation) and ImageJ (http://rsbweb.nih.gov/ij/). Sensor calibration (pH 3–10, single pH steps) was performed at
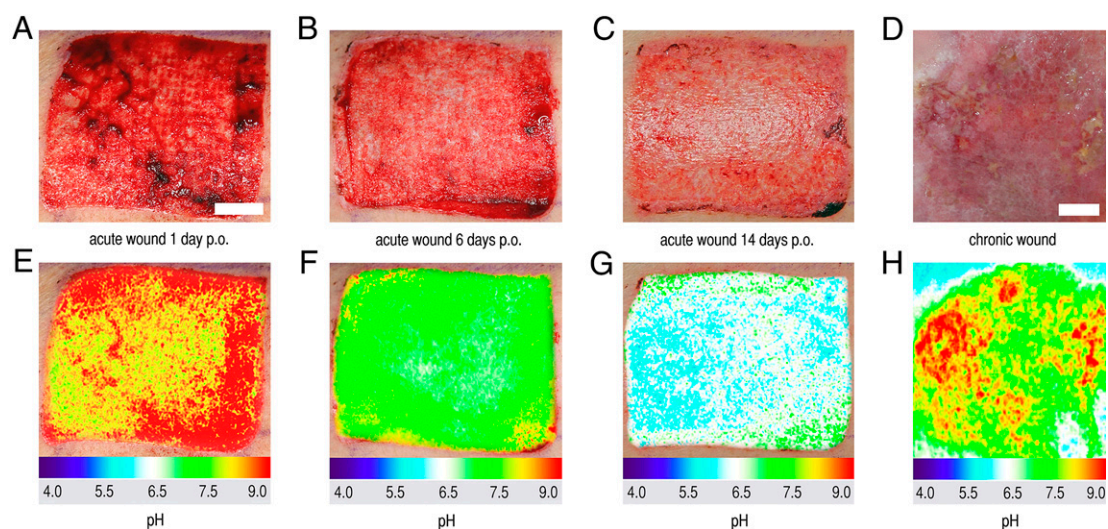
Fig. 4. Luminescence imaging of pH during cutaneous wound healing. (*A–C*) Wound healing of split-thickness (∼400 μm) skin-graft donor sites on days (*A*) 1 (inflammation), (*B*) 6 (granulation), and (*C*) 14 (reepithelialization) after split-skin harvesting. (*E–G*) Respective pseudocolor images created with optical 2D pH sensors. Wound healing is reflected by decreasing pH values. (*D* and *H*) Chronic venous ulcer (*D*) on the medial ankle and the respective pH distribution (*H*). Different stages of healing within this wound (inflammation and granulation) and surrounding intact skin (e.g., upper left and right corners) are visualized. The colors allow an easy correlation with the wound-healing phases as shown for physiological healing (*E–G*). p.o., postoperatively. (Scale bars, 1 cm.)

20–40 °C (5 °C steps) with varying oxygen concentrations (0–20% oxygen in argon at 5% steps).

Cytotoxicity and Cellular Uptake. Experiments are described in *SI Materials and Methods*.

Study Subjects. Details are given in *SI Materials and Methods*.

In Vivo Luminescence Imaging. Sensor foils were gently applied to the skin or wound surface (starting from one margin) and were allowed to slowly adapt to tissue surfaces caused by adhesion forces. This technique prevents the inclusion of air bubbles underneath the foils during application, thereby ensuring uniform contact between sensors and tissues. No pressure was applied to the foils during measurements. For SC pH gradient measurements (31), we removed the SC from the volar forearm with 100 tape strippings. 3M Scotch Ruban adhesive tape (4 cm²; 3M) was pressed firmly against the skin for 3 s and then, swiftly pulled away. The SC was removed down to the stratum granulosum, which appeared as a glistening layer (31). Temperature and humidity were kept constant. We recorded pH after every 10 strippings, and we measured pH in split-skin donor site wounds 1, 6, and 14 d after split-skin harvesting. For the first 6 d, Tielle (in case of extensive exudation, Tielle-Plus; Johnson & Johnson) was used as wound dressing and subsequently replaced by Mepilex (Mölnlycke Healthcare GmbH), which remained on the donor site from day 6 to 14 postoperatively. We recorded pH using the 2D

sensor foils covering the entire wound surface (time from application to removal of foils < 5 min). For measurements [distance from camera to stripping site was 8 (SC gradient) or 30 cm (split-skin wounds) and was focus-controlled], we used data from standard-sized squares (100 × 100 pixels) from the exact spot where the glass electrode had been placed to measure pH. 2D pseudocolor pH images of the entire wounds were also obtained. No residual luminescence was detected after removal of the sensor foils, confirming that there was no leakage of sensor particles.

Statistics. Statistics are described in *SI Materials and Methods*.

1. Lee D, et al. (2007) In vivo imaging of hydrogen peroxide with chemiluminescent nanoparticles. *Nat Mater* 6:765–769.
2. Nagai T, Sawano A, Park ES, Miyawaki A (2001) Circularly permuted green fluorescent proteins engineered to sense Ca²⁺. *Proc Natl Acad Sci USA* 98:3197–3202.
3. Nagai T, Yamada S, Tominaga T, Ichikawa M, Miyawaki A (2004) Expanded dynamic range of fluorescent indicators for Ca²⁺ by circularly permuted yellow fluorescent proteins. *Proc Natl Acad Sci USA* 101:10554–10559.
4. Nakai J, Ohkura M, Imoto K (2001) A high signal-to-noise Ca²⁺ probe composed of a single green fluorescent protein. *Nat Biotechnol* 19:137–141.
5. Niethammer P, Grabher C, Look AT, Mitchison TJ (2009) A tissue-scale gradient of hydrogen peroxide mediates rapid wound detection in zebrafish. *Nature* 459:996–999.
6. Zhang G, Palmer GM, Dewhirst MW, Fraser CL (2009) A dual-emissive-materials design concept enables tumour hypoxia imaging. *Nat Mater* 8:747–751.
7. Bowyer WJ, Xu W, Demas JN (2009) Determining proton diffusion in polymer films by lifetimes of luminescent complexes measured in the frequency domain. *Anal Chem* 81:378–384.
8. Liebsch G, Klimant I, Krause C, Wolfbeis OS (2001) Fluorescent imaging of pH with optical sensors using time domain dual lifetime referencing. *Anal Chem* 73:4354–4363.
9. Walpole GS (1914) An improved hydrogen electrode. *Biochem J* 8:131–133.
10. Bassnett S, Reinisch L, Beebe DC (1990) Intracellular pH measurement using single excitation-dual emission fluorescence ratios. *Am J Physiol* 258:C171–C178.
11. Chen Y, Arriaga EA (2006) Individual acidic organelle pH measurements by capillary electrophoresis. *Anal Chem* 78:820–826.
12. Deriy LV, et al. (2009) Disease-causing mutations in the cystic fibrosis transmembrane conductance regulator determine the functional responses of alveolar macrophages. *J Biol Chem* 284:35926–35938.
13. Behne MJ, et al. (2002) NHE1 regulates the stratum corneum permeability barrier homeostasis. Microenvironment acidification assessed with fluorescence lifetime imaging. *J Biol Chem* 277:47399–47406.
14. Carlsson K, Liljeborg A (1998) Simultaneous confocal lifetime imaging of multiple fluorophores using the intensity-modulated multiple-wavelength scanning (IMS) technique. *J Microsc* 191:119–127.
15. Niesner R, et al. (2005) 3D-resolved investigation of the pH gradient in artificial skin constructs by means of fluorescence lifetime imaging. *Pharm Res* 22:1079–1087.
16. Gallagher FA, et al. (2008) Magnetic resonance imaging of pH in vivo using hyperpolarized 13C-labelled bicarbonate. *Nature* 453:940–943.
17. Gillies RJ, Liu Z, Bhujwalla Z (1994) 31P-MRS measurements of extracellular pH of tumors using 3-aminopropylphosphonate. *Am J Physiol* 267:C195–C203.
18. van Sluis R, et al. (1999) In vivo imaging of extracellular pH using 1H MRSI. *Magn Reson Med* 41:743–750.
19. Winter GD (1962) Formation of the scab and the rate of epithelization of superficial wounds in the skin of the young domestic pig. *Nature* 193:293–294.
20. Hunt TK, Twomey P, Zederfeldt B, Dunphy JE (1967) Respiratory gas tensions and pH in healing wounds. *Am J Surg* 114:302–307.
21. Schreml S, et al. (2010) The impact of the pH value on skin integrity and cutaneous wound healing. *J Eur Acad Dermatol Venereol* 24:373–378.
22. Singer AJ, Clark RA (1999) Cutaneous wound healing. *N Engl J Med* 341:738–746.
23. Schreml S, Szeimies R-M, Prantl L, Landthaler M, Babilas P (2010) Wound healing in the 21st century. *J Am Acad Dermatol* 63:866–881.
24. Bickers DR, et al. (2006) The burden of skin diseases: 2004 a joint project of the American Academy of Dermatology Association and the Society for Investigative Dermatology. *J Am Acad Dermatol* 55:490–500.
25. (1992) Tumour pH. *Lancet* 340:342–343.
26. Vaupel P, Kallinowski F, Okunieff P (1989) Blood flow, oxygen and nutrient supply, and metabolic microenvironment of human tumors: A review. *Cancer Res* 49:6449–6465.
27. Devanathan S, Dahl TA, Midden WR, Neckers DC (1990) Readily available fluorescein isothiocyanate-conjugated antibodies can be easily converted into targeted phototoxic agents for antibacterial, antiviral, and anticancer therapy. *Proc Natl Acad Sci USA* 87:2980–2984.
28. Barretto RP, Messerschmidt B, Schnitzer MJ (2009) In vivo fluorescence imaging with high-resolution microlenses. *Nat Methods* 6:511–512.
29. Kwan AS, Barry C, McAllister IL, Constable I (2006) Fluorescein angiography and adverse drug reactions revisited: The Lions Eye experience. *Clin Experiment Ophthalmol* 34:33–38.
30. Yannuzzi LA, et al. (1986) Fluorescein angiography complication survey. *Ophthalmology* 93:611–617.
31. Ohman H, Vahlquist A (1994) In vivo studies concerning a pH gradient in human stratum corneum and upper epidermis. *Acta Derm Venereol* 74:375–379.
32. Bland JM, Altman DG (1986) Statistical methods for assessing agreement between two methods of clinical measurement. *Lancet* 1:307–310.
33. Gurtner GC, Werner S, Barrandon Y, Longaker MT (2008) Wound repair and regeneration. *Nature* 453:314–321.
34. Schugart RC, Friedman A, Zhao R, Sen CK (2008) Wound angiogenesis as a function of tissue oxygen tension: A mathematical model. *Proc Natl Acad Sci USA* 105:2628–2633.
35. Xue C, Friedman A, Sen CK (2009) A mathematical model of ischemic cutaneous wounds. *Proc Natl Acad Sci USA* 106:16782–16787.
36. Cork MJ, et al. (2009) Epidermal barrier dysfunction in atopic dermatitis. *J Invest Dermatol* 129:1892–1908.
37. Davey KR (1994) Modelling the combined effect of temperature and pH on the rate coefficient for bacterial growth. *Int J Food Microbiol* 23:295–303.
38. Olson ER (1993) Influence of pH on bacterial gene expression. *Mol Microbiol* 8:5–14.
39. Tolba MK, Saleh AM (1954) Correlation between pH-value of tomato tissue and its susceptibility to attack by two Fusaria. *Nature* 173:87.
40. Kürner JM, et al. (2001) Inert phosphorescent nanospheres as markers for optical assays. *Bioconjug Chem* 12:883–889.
41. Borisov S, Vasylevska A, Krause C, Wolfbeis OS (2006) Composite luminescent material for dual sensing of oxygen and temperature. *Adv Funct Mater* 16:1536–1542.
42. Wolfbeis OS (2008) Sensor paints. *Adv Mater* 20:3759–3763.
43. Stich MIJ, Fischer LH, Wolfbeis OS (2010) Multiple fluorescent chemical sensing and imaging. *Chem Soc Rev* 39:3102–3114.

MEDICAL SCIENCES

CHEMISTRY